



# Multi-Method Analysis of Porosity in L-PBF AISI 316L-2.5Cu Alloy: Correlation of Processing Parameters and Defect Characterization

Sanae Tajalli<sup>1,2</sup> · Alireza Moradi<sup>3</sup> · Amir Behjat<sup>4,5</sup> · Abdollah Saboori<sup>4,5</sup> · Luca Iuliano<sup>4,5</sup>

Received: 11 November 2025 / Revised: 7 March 2026 / Accepted: 22 March 2026  
© The Author(s) 2026

## Abstract

In recent years, laser powder bed fusion (L-PBF) has become an interesting method for producing metal components with complex shapes. However, L-PBF can lead to defects like porosity, affecting the quality and reliability of the final components. This study investigates the structural defects and relative density of AISI 316L stainless steel with 2.5 wt.% Cu fabricated via L-PBF under varying processing parameters. The relative density of the samples was evaluated using a combination of optical microscopy (OM), Archimedes density method, and x-ray computed tomography (XCT), allowing for a comprehensive analysis of defect morphology, including pore size, shape, and distribution. The primary objective of this research is to compare the accuracy and effectiveness of these three density measurement methods, which have not been widely compared for this specific alloy. The results show differences between the methods, with XCT providing a 3D perspective of porosity, OM providing detailed 2D surface analysis, and the Archimedes method being sensitive to surface defects and cracks. These findings highlight the importance of selecting appropriate measurement techniques for evaluating the quality of additive manufacturing parts and highlight the influence of processing parameters on defect formation and density.

**Keywords** Additive manufacturing · Laser powder bed fusion · Density · AISI 316L · Tomography

## Introduction

Metal additive manufacturing (AM) has evolved as a revolutionary method for fabricating metal components. This advanced process involves precise layering and melting of materials to construct complex shapes [1, 2]. In recent

years, metal AM has emerged as a viable alternative to conventional industrial production methods. It has distinctive advantages, such as the capacity to generate complex geometries, manufacture customized components, construct multi-material parts, eliminate assembly needs, and significantly reduce material waste [3, 4]. Moreover, in Industry 4.0 and smart manufacturing, metal AM has gained prominence through the integration of artificial intelligence-driven design, Internet of Things-enabled remote access, and highly efficient automated control systems [5]. The categorization of metal AM techniques encompasses five principal types, including powder bed fusion (PBF), directed energy deposition (DED), sheet lamination (SL), metal binder jetting (MBJ), and material extrusion (ME) [6]. PBF utilizes laser or electron beams to selectively melt metal powder layers, whereas DED uses a concentrated energy source to deposit molten metal gradually. SL constructs components by layering and adhering metal sheets, while MBJ uses a binder to selectively unite layers of metal powder. Understanding these classifications helps researchers and engineers to select and optimize the most suitable metal AM technique for their particular applications. Each method presents unique

✉ Abdollah Saboori  
abdollah.saboori@polito.it; saboori1985@yahoo.com

<sup>1</sup> Department of Applied Science and Technology, Politecnico di Torino, Corso Duca Degli Abruzzi 24, 10129 Torino, Italy

<sup>2</sup> Department of Engineering Science, University West, 461 86 Trollhättan, Sweden

<sup>3</sup> Department of Mechanical and Aerospace Engineering, Politecnico di Torino, Corso Duca Degli Abruzzi 24, 10129 Torino, Italy

<sup>4</sup> Department of Management and Production Engineering, Politecnico di Torino, Corso Duca degli Abruzzi 24, 10129 Torino, Italy

<sup>5</sup> Integrated Additive Manufacturing Center (IAM@PoliTo), Politecnico di Torino, Corso Castelfidardo 51, 10129 Torino, Italy

advantages and limitations, making it essential to carefully select the most suitable process based on the specific requirements of the application [7–11].

Laser powder bed fusion (L-PBF) is a widely used AM process [12, 13]. It facilitates the fabrication of metallic components using diverse material powders, such as titanium alloys [14, 15], aluminum alloys [16, 17], and stainless steel [18, 19]. Although L-PBF technology has advanced, it still faces several limitations that constrain its application. These include limited available materials, low process efficiency, and structural defects in the produced parts, all of which hinder the broader adoption of L-PBF [20–22]. Moreover, different characteristics of the L-PBF process significantly influence the formation of structural defects in printed components [22, 23]. Among the different alloys used in L-PBF, AISI 316L is one of the most important alloys in the biomedical and surgical industries due to its excellent performance [24–26]. Yet, it remains susceptible to localized corrosion and inflammation in long-term physiological conditions [27, 28]. To overcome these limitations, 2.5 wt.% Cu was incorporated to leverage its reported ability to enhance corrosion resistance and provide essential antibacterial effects through the release of Cu ions [19, 29]

The primary microstructural defects associated with L-PBF include gas-induced porosity (GIP), lack of fusion (LOF), keyhole (KH), and balling phenomena. GIPs are typically spherical, small, and uniformly distributed throughout the specimen. Gas porosities form when gases entrapped in the melt pool during rapid solidification are unable to move out. This can occur due to elevated temperatures, reduced powder bed density, gas atomization, laser-induced evaporation, or the presence of surface contaminants such as oxides and moisture [30]. In contrast, LOF defects are irregular in shape and larger and often found at the surface or interior layers. LOF defects occur due to the incomplete fusion of adjacent layers, which is associated with insufficient laser energy input [31], material shrinkage during solidification [32], or poor bonding resulting from oxidation, which affects the wetting angle between layers [33]. KH defects occur under high-power, low-scan-speed conditions and are characterized by deep, narrow vapor voids. Unlike GIP or LOF, excessive energy input in L-PBF leads to material evaporation, plasma generation, and significant laser penetration, which produces KH porosity [34]. Balling refers to coarsened spherical formations on the surface featuring interrupted dendritic structures. Balling occurs at high scan speeds, causing an elongated melt pool to break into small beads due to surface tension instability. Low energy input leads to coarser beads, while oxide layers or moisture on the powder surface disrupt surface tension, also contributing to balling [35].

Although the primary causes of these defects have been discussed, it is important to note that additional factors may also contribute to their formation. GIP is primarily related to raw materials and is generally difficult to eliminate through process optimization. Other defects, such as LOF, KH, and balling, are typically caused by inappropriate process parameters [36]. These issues can often be addressed by optimizing factors such as oxygen content, scanning speed, laser power, fluidity, and wettability of the molten material in the melt pool [37].

Various techniques are employed to analyze defects in components produced by L-PBF [38]. The metallographic and Archimedes methods are among the most popular approaches, each having unique advantages and limits. Although the metallographic approach is time-consuming and destructive, this approach is highly efficient for analyzing microstructural characteristics. The accuracy of the analysis depends on the quality of the cross-sectional preparation and the magnification used. Roth et al. [39] analyzed a cross section of a NiCu-based alloy sample to investigate porosity caused by unoptimized process parameters. They identified defects as LOF and unmelted powder (due to low energy density) and fine KHs (due to high energy density), highlighting the impact of energy input on defect formation. Moreover, Men et al. [40] used optical microscopy (OM) and image analysis to examine the longitudinal cross section of WE43 magnesium alloys, revealing microstructural formations and void defects that appeared as isolated or continuous lines along adjacent scales.

Conversely, the Archimedes method is a nondestructive technique that provides measurements of the relative density of samples. However, it cannot provide details on the shape, distribution, or placement of porosities within the material. For example, Yamamoto et al. [41] used the Archimedes method to measure the density of pure tungsten specimens. However, they noted that surface cracks reduced their accuracy by affecting the penetration of the liquid due to surface tension. To address this, they also applied an image analysis method, using an optical microscope to measure the area ratio of defects on polished cross sections, providing a more reliable density estimate that is less influenced by surface cracks. Moreover, Zheng et al. [38] employed the Archimedes method to measure the density of AISI 316L stainless steel samples, evaluating the impact of L-PBF processing parameters on density. To provide a more comprehensive analysis, they also compared these bulk density measurements with data obtained through x-ray computed tomography (XCT) and OM.

XCT analyzes microstructural defects in L-PBF components by using different methods to create 3D models from multiple x-ray images taken around a rotating axis [42]. However, integrating different methodologies,

such as Archimedes method and OM, can provide a more comprehensive understanding of defects and their impact on material performance. XCT overcomes limitations by providing a nondestructive means to analyze the internal structure of materials. XCT also provides detailed spatial information about micro-defects, including the distribution of pores, cracks, and inclusions, as well as other structural defects. This method is robust and widely used to visualize and evaluate internal defects in materials [22]. For instance, Poudel et al. [43] used XCT scans to analyze volumetric defects in L-PBF samples. Defects were visually classified by experts into three types (LOF, GEP, KH), with 1970 out of 2156 defects conclusively labeled. These labeled defects were used to train classification models, ensuring reliable defect pattern recognition. Additionally, Wang et al. [44] use high-resolution XCT to quantify pore size, sphericity, orientation, and porosity in L-PBF 316L built under five energy-density settings, and they compare these XCT-derived pore statistics before versus after tensile testing to relate measurement to mechanical response. To validate the accuracy of XCT evaluation, Jolley et al. [45] used mechanical polishing serial sectioning as a high-resolution ground truth to assess XCT measurements in Ti-6Al-4 V built via L-PBF. Their correlative analysis revealed that XCT tended to overestimate the equivalent spherical diameter of larger pores while failing to resolve finer porosity distributions that were clearly distinct in the optical serial-sectioning data. These findings underscore the limitations of relying solely on XCT for quantitative defect characterization and highlight the need for multimodal validation to ensure structural integrity. In another work done by Jolley et al. [46], a comprehensive comparative analysis involving multiple XCT systems and post-processing workflows was recently conducted to quantify measurement uncertainty. Their results highlighted that XCT-derived porosity metrics are highly sensitive to experimental variables, with global volume fractions varying by 40% to 60% relative to serial-sectioning benchmarks. Crucially, they found that the contrast-to-noise ratio (CNR) often played a more decisive role in segmentation accuracy than spatial resolution alone, as datasets with low CNR frequently resulted in the significant undersizing or complete omission of pores regardless of whether commercial or open-source computational workflows were employed.

In this study, AISI 316L stainless steel with 2.5 wt.% Cu samples was produced using L-PBF to examine defects under various processing parameters. The relative density of the samples was evaluated through a combination of OM, Archimedes density measurements, and XCT. This comprehensive approach allowed for a detailed analysis of defect morphology, including sphericity, volume, and porosity sizes, providing insights into their relationship with processing conditions. A key objective of this research

is to compare the accuracy and effectiveness of these three density measurement methods, which have not been extensively studied for this alloy. Significant differences were observed, with XCT providing a 3D perspective of pore distribution. At the same time, OM provided 2D defect evaluation, and the Archimedes method measured bulk density but was influenced by surface cracks and porosity. The study also analyzed the reasons behind these differences and their consequences for density measurement, aiming to identify optimal conditions for higher quality in components.

## Materials and Methods

### Sample Building

The 71 cubic samples (8 mm × 8 mm × 8 mm) were produced using the PrintSharp 250 L-PBF machine with 71 different process parameters. As shown in Fig. 1, the feedstock consisted of 2.5 wt.% Cu and AISI 316L mixture and spun at 60 rpm for 12 h using tumbler mixer. The mixing parameters were determined following a homogeneity assessment using a scanning electron microscope (SEM). Being fully blended means that individual powders are uniformly mixed with a homogenous distribution before melting.

The data show that the average particle sizes of the starting AISI 316L-2.5Cu powders are 27 μm ( $d_{10} = 13$  μm,  $d_{50} = 23$  μm,  $d_{90} = 40$  μm) and 6.3 μm ( $d_{10} = 3.1$  μm,  $d_{50} = 5.3$  μm,  $d_{90} = 13.1$  μm), respectively. The chemical composition and morphology were analyzed using energy-dispersive x-ray spectroscopy (EDS), see Table 1. After printing, the components were cut from the build platform using wire electron discharge machining (WEDM).

A total of 71 experimental data points were selected to cover a wide range of three main process parameters, including laser power ( $P$ ), laser speed ( $v$ ), and hatch distance ( $h$ ), as outlined in Table 2. The parameters were chosen based on prior experience with the machine and a private initial evaluation. Laser power ranged from 100 to 340 W, scan speed varied between 400 and 1000 mm/s, and hatch distance was set between 0.1 and 0.2 mm. The extensive parameter range led to considerable variance in volumetric energy density (VED), which quantifies the energy input per unit volume. VED, which is mentioned in Eq. (1), is widely used for evaluating the densification behavior of materials manufactured by L-PBF [47].

$$\text{VED} = P / v.h.t \quad (1)$$

where  $P$ ,  $v$ , and  $h$  represent power, scan speed, and hatch distance, respectively. In Eq. (1),  $t$  also indicates the layer thickness, which was set to 0.03 mm in this study.

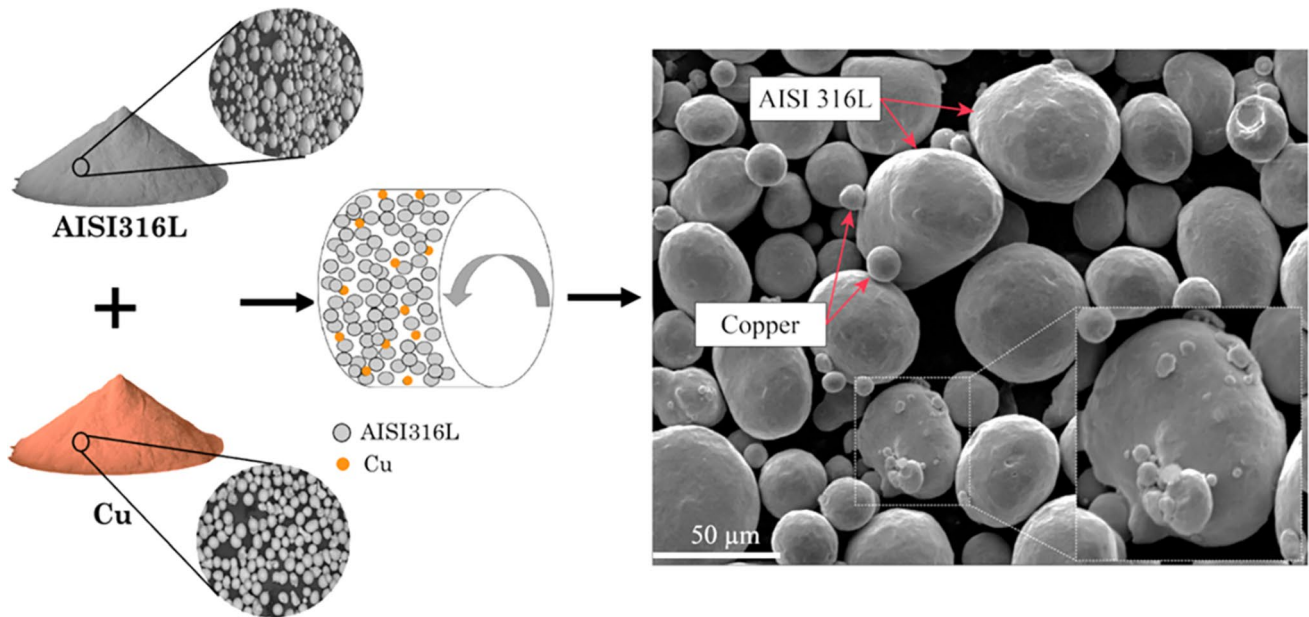


**Fig. 1.** Mixing schematic, morphology, and particle size distribution of the mixed 316L stainless steel with 2.5 wt% of copper

**Table 1.** The chemical composition of the combined AISI316L-Cu powder by two different analyses

Elements	Cr	Ni	Mo	C	Mn	Cu	P
Nominal (wt.%)	17-19	13-15	2.25-3	0.03	2.0	2.5	25
Analyzed (wt%)	17.02	13.5	2.04	0.02	2.11	2.92	22

## Sample Characterization

The Archimedes method, following ASTM F3637-23 [48], was used to measure the relative density and total porosity of the samples by weighing them in air (dry weight), fully immersed in distilled water (immersed weight), and after water absorption (wet weight). The schematic of this measurement is shown in Fig. 2(a). Distilled water with a density of 0.997 g/cm<sup>3</sup> was used as the liquid medium. Theoretical density (7.985 g/cm<sup>3</sup>) was calculated based on the composition of the material using the theoretical rule of mixtures. Total porosity and relative density were computed using established formulas, determined as:

$$\rho_{\text{Archimedes}} = \rho_{\text{liquid}} \times \frac{W_{\text{dry}}}{W_{\text{dry}} - W_{\text{immersion}}} \quad (2)$$

$$\rho_{\text{Geometrical}} = \rho_{\text{liquid}} \times \frac{W_{\text{dry}}}{W_{\text{wet}} - W_{\text{immersion}}} \quad (3)$$

$$\text{Total porosity percentage} = \frac{\rho_{\text{theoretical}} - \rho_{\text{bulk}}}{\rho_{\text{theoretical}}} \times 100\% \quad (4)$$

$$\text{Relative Density percentage} = \frac{\rho_{\text{Archimedes}}}{\rho_{\text{theoretical}}} \times 100\% \quad (5)$$

The terms  $\rho_{\text{Archimedes}}$  and  $\rho_{\text{Geometrical}}$  refer to the Archimedes density (apparent density) and the geometrical density (bulk density), respectively.

Given that the Archimedes method is a rapid and effective methodology for porosity determination, two additional density measurement methods, including XCT and image analysis, were also employed on selected samples. This comparison aimed to determine whether the Archimedes approach provides sufficiently precise data to serve as a rapid technique for measuring density and to assess its reliability against more comprehensive and time-intensive methodologies. To achieve this, eleven samples were selected for XCT analysis within a defined range of VEDs after applying the Archimedes method. The selection aimed to cover a wide range of VEDs, including samples with low, medium, and high VEDs, to obtain a comprehensive analysis and improve the accuracy of the results. Subsequently, the tomographic investigation yielded significant information on the distribution, geometry, diameters, and other critical porosity characteristics.

**Table 2.** Process parameters for AISI316L–2.5%Cu used in the design of experiment

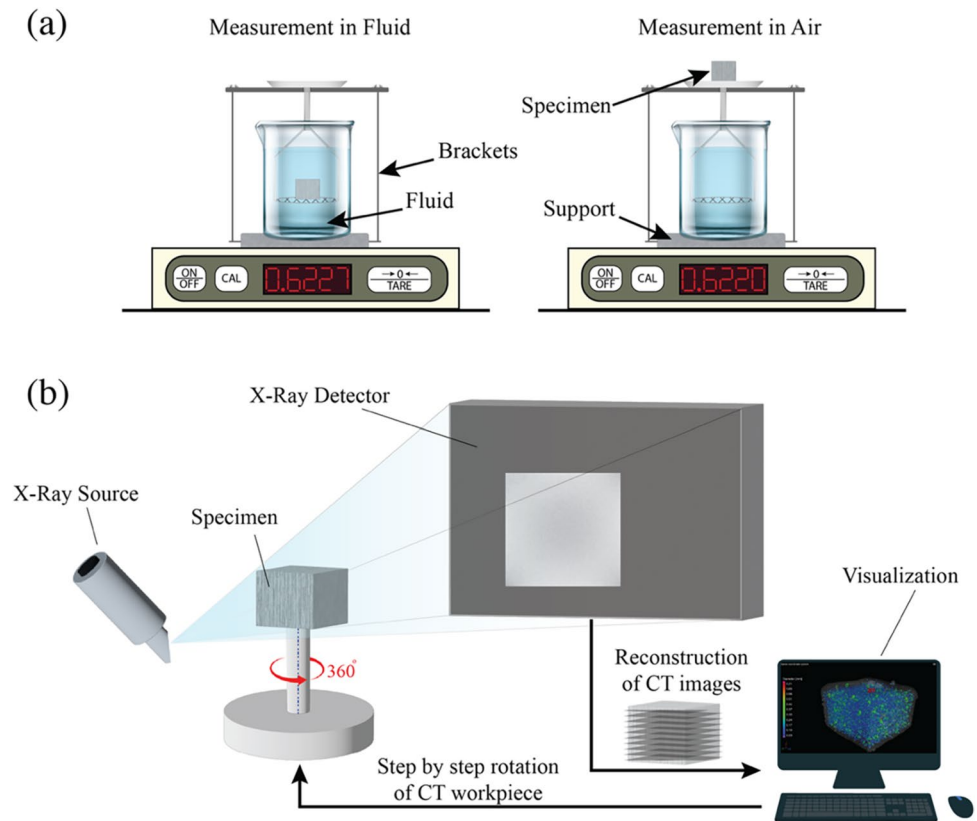
S.ID	Power (W)	Scan Speed (mm/s)	Hatch Distance (mm)	VED (J/mm <sup>3</sup> )	S.ID	Power (W)	Scan Speed (mm/s)	Hatch Distance (mm)	VED (J/mm <sup>3</sup> )
1	100	1000	0.1	33.33	37	190	600	0.12	87.96
2	100	800	0.1	41.66	38	190	800	0.12	65.97
3	150	1000	0.12	41.66	39	190	1000	0.12	52.77
4	190	400	0.1	158.33	40	200	400	0.12	138.88
5	190	600	0.1	105.55	41	200	600	0.12	92.59
6	190	800	0.1	79.16	42	200	800	0.12	69.44
7	190	1000	0.1	63.33	43	200	1000	0.12	55.55
8	200	400	0.1	166.66	44	200	1000	0.11	60.60
9	200	600	0.1	111.11	45	270	400	0.11	204.54
10	200	800	0.1	83.33	46	270	400	0.12	187.50
11	200	1000	0.1	66.66	47	270	600	0.12	125.00
12	270	400	0.1	225.00	48	270	800	0.12	93.75
13	270	600	0.1	150.00	49	270	1000	0.12	75.00
14	270	800	0.1	112.50	50	340	400	0.12	236.11
15	270	1000	0.1	90.00	51	340	600	0.12	157.40
16	340	400	0.1	283.33	52	340	800	0.12	118.05
17	340	600	0.1	188.88	53	340	1000	0.12	94.44
18	340	800	0.1	141.66	54	190	400	0.13	121.79
19	340	1000	0.1	113.33	55	190	600	0.13	81.19
20	190	400	0.11	143.93	56	190	800	0.13	60.89
21	190	600	0.11	95.95	57	190	1000	0.13	48.71
22	190	800	0.11	71.96	58	190	1000	0.13	48.71
23	190	1000	0.11	57.57	59	200	400	0.13	128.20
24	200	400	0.11	151.51	60	200	600	0.13	85.47
25	200	600	0.11	101.01	61	200	800	0.13	64.10
26	200	800	0.11	75.75	62	200	1000	0.13	51.28
27	200	1000	0.11	60.60	63	270	400	0.13	173.07
28	270	400	0.11	204.54	64	270	600	0.13	115.38
29	270	600	0.11	136.36	65	270	800	0.13	86.53
30	270	800	0.11	102.27	66	270	1000	0.13	69.23
31	270	1000	0.11	81.81	67	270	1000	0.2	45.00
32	340	400	0.11	257.57	68	340	400	0.13	217.94
33	340	600	0.11	171.71	69	340	600	0.13	145.29
34	340	800	0.11	128.78	70	340	800	0.13	108.97
35	340	1000	0.11	103.03	71	340	1000	0.13	87.17
36	190	400	0.12	131.94					

The XCT process started by placing each sample on the holder, as shown in Fig. 2(b), with a copper filter positioned in front of the x-ray source and the monitor detector. The sample position was verified and adjusted using specialized software for precise alignment. After confirming alignment, tomography proceeded. The resulting scans provided high-resolution information about the internal structure of each sample, enabling a thorough evaluation of porosity features.

Subsequent to the XCT analysis, the samples were subjected to metallographic preparation for the examination of

their polished cross sections using an OM. The grinding process utilized a Presi machine with abrasive papers (P480, P600, P800, P1200, and P2400). Subsequent to grinding, polishing was executed utilizing 1-micron and 3-micron grit polishing pads. This thorough preparation allowed accurate visualization of porosity and microstructural characteristics for further investigation. After polishing, the samples were analyzed utilizing a LEICA optical microscope. Subsequently, the ImageJ software quantified porosity percentages, pore sizes, and their distributions. This additional

**Fig. 2.** **a** Schematic of the Archimedes method for measuring density and porosity, **b** setup for XCT analysis, showing the placement of the sample on the holder with a copper filter in front of the x-ray source and the monitor detector for accurate alignment



study provided insights regarding superficial flaws and their relationship with the volumetric data acquired from XCT. The integration of these methodologies facilitated a thorough comprehension of porosity features, linking surface and volumetric observations to confirm findings across various scales.

The specimens for microstructural analysis were initially subjected to mechanical grinding using sandpapers with grit sizes ranging from 180 to 4000 mesh, followed by polishing with a 1  $\mu\text{m}$  and 0.3  $\mu\text{m}$  diamond paste. Thereafter, the specimens were electrolytically etched in a solution containing 65% nitric acid for 20 seconds at an applied voltage of 10 V and immediately rinsed with alcohol to enhance the visibility of microstructure. Microstructural observations were conducted using a scanning electron microscope (SEM, Philips XL30).

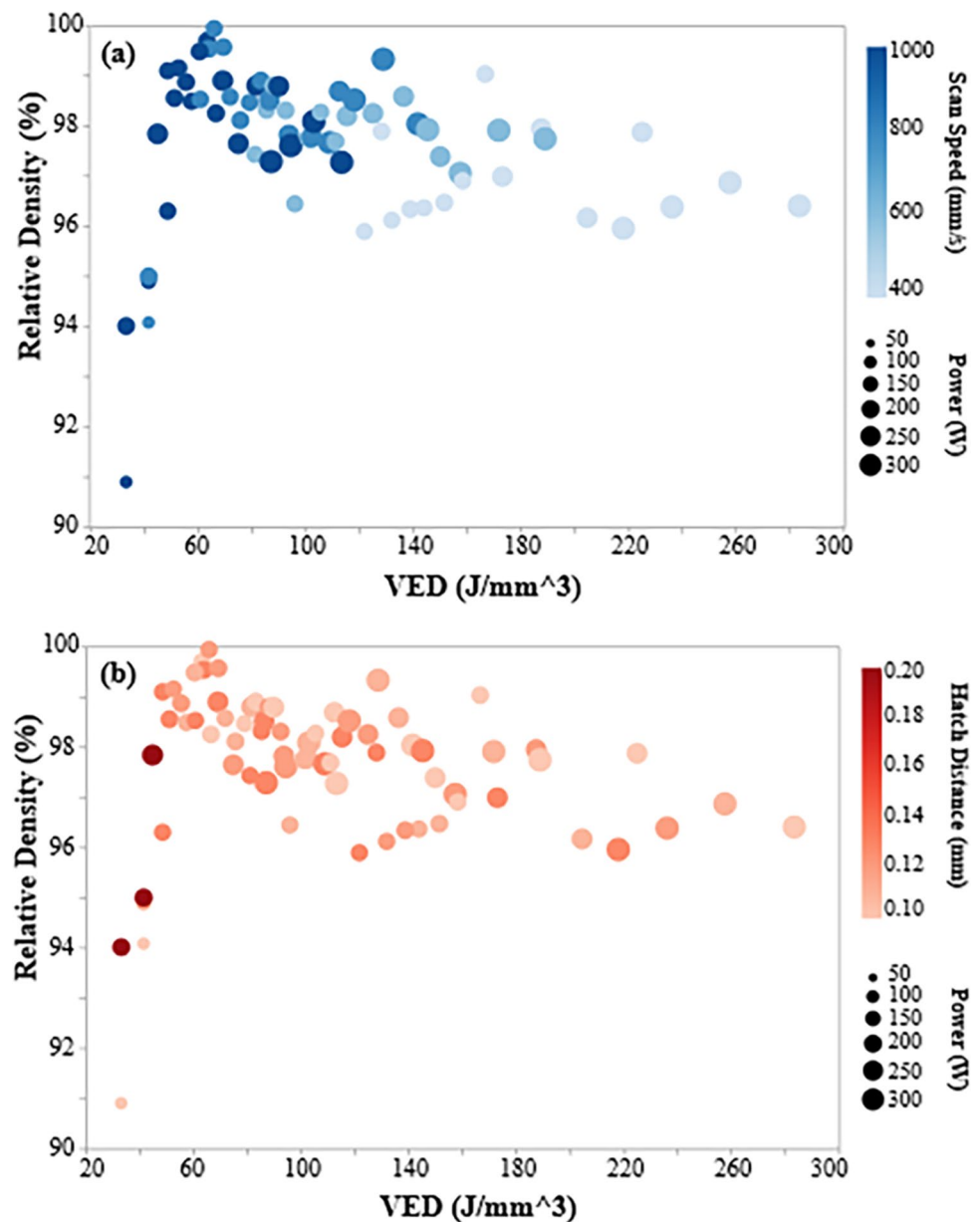
## Results and Discussion

### Archimedes Method

The correlation between process parameters and relative density is a key factor in AM, as it directly influences the mechanical performance and quality of the components [49]. To analyze these effects, the relative density of all samples

is plotted against VED in Fig. 3 (a) and (b). In Fig. 3 (a), the color intensity of the data points represents the scan speed, while the circle size indicates the laser power. As VED increases, the relative density rises steadily, reaching about 0.99 at approximately  $70 \text{ J/mm}^3$ , after which it generally declines. However, a secondary increasing trend appears between roughly 100 and  $130 \text{ J/mm}^3$ , followed by a decrease again at higher VED values. Lower scan speeds (darker points) show higher relative densities since slower speeds provide sufficient energy absorption to melt the powder. Conversely, higher speeds (brighter points) produce lower densities due to poor energy transfer. Higher laser powers, indicated by larger circles, typically improve density; however, excessive power can cause problems, including material expulsion or over melting. A similar plot is shown in Fig. 3 (b), where color intensity indicates hatch distance and circle size shows laser power. Lower hatch distances (darker points) indicate higher relative densities, while higher hatch distances (brighter points) correspond to reduced densities, most likely due to inadequate layer bonding. Larger circles represent higher power and improve density to an optimal point above which too excessive energy may cause instabilities. These results highlight the effect of scan speed, hatch distance, and laser power on the relative density of samples. The results highlight that inadequate or excessive input energy might cause problems, showing the importance of

**Fig. 3.** Relationship between VED and relative density of samples. **a** Data points are colored by scan speed and sized by laser power. **b** Data points are colored by hatch distance and sized by laser power

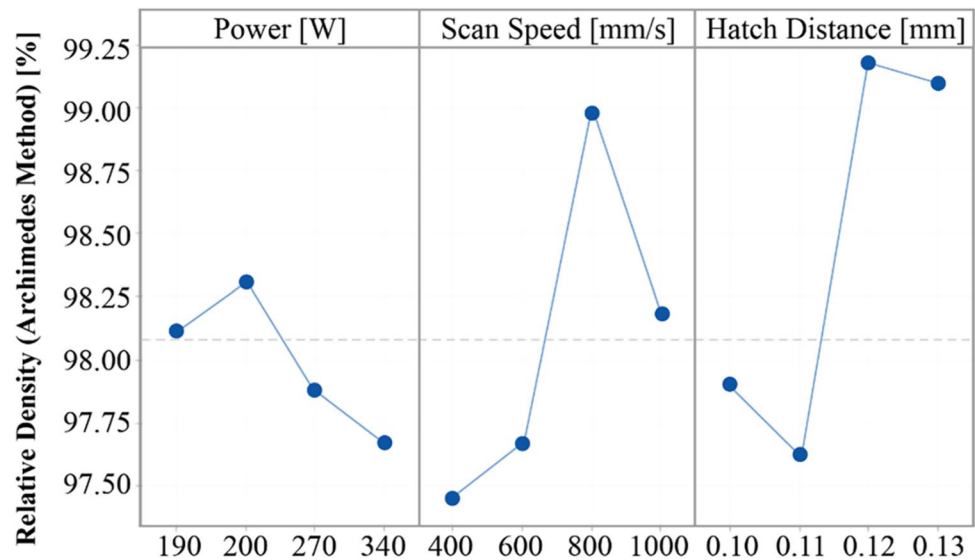


process parameter optimization for minimizing defect content and improving mechanical properties [50].

Based on data acquired by the Archimedes method, the main effects plot for relative density, in Fig. 4, illustrate the influence of three key process parameters, power, scanning speed, and hatch distance, on relative density. Among these characteristics, hatch distance has the most significant impact on relative density, as shown by the sharp trend in Fig. 4 (c). When the hatch distance reaches 0.12 mm, there is a significant increase in relative density. However, as the hatch distance exceeds 0.12 mm, a slight decrease in density occurs. This decrease is likely due to insufficient overlap, which can cause defects such as LOF [51]. Although scan speed has less effect than hatch distance, it

still considerably affects defect content. At reduced scan speeds, such as 400 mm/s, the relative density is low, due to high input energy that may result in defects such as KHs or GIPs [52]. As the scanning speed increases to 800 mm/s, relative density markedly enhances, reaching its maximum level. This optimal range balances energy input and material solidification, resulting in the highest density [53]. However, an additional increase in scan speed to 1000 mm/s decreases the relative density, suggesting that higher speed may yield insufficient energy density, resulting in inadequate melting between layers [52]. The influence of power on relative density is lower than speed and hatch distance. A rise in power from 190 W to 200 W results in a slight increase in relative density, indicating improved melting. However, a

**Fig. 4.** Main effects plot highlighting optimal process parameters for achieving maximum relative density



considerable decrease in relative density is observed as the power rises to 270 W and 340 W. This trend implies that higher power levels may cause overheating or vaporization, resulting in defects such as KHs [54].

### XCT and Image Analysis

XCT is a nondestructive method that provides highly accurate measurements of material density. This provides important advantages over traditional techniques. XCT also allows for detailed analysis of pore distribution, size, shape, and geometry. These analyses are critical for understanding material quality and performance [55]. By using shape indicators like sphericity and compactness, XCT provides valuable insights into the microstructure, aiding in process optimization and quality control. Sphericity, the first shape indicator, measures how closely the shape of a pore resembles a sphere. It is defined as the ratio of the surface area of a sphere with the same volume as the pore to the surface area of the pore, where  $V_{\text{pore}}$  is the pore volume and  $A_{\text{pore}}$  is the pore surface area. As it is illustrated by Eq. (6):

$$\Psi = \frac{\pi^{\frac{1}{3}} (6 \cdot V_{\text{pore}})^{\frac{2}{3}}}{A_{\text{pore}}} \quad (6)$$

Another shape indicator is compactness, which describes the relationship between volume of the pore and the volume of a sphere with a diameter equal to the maximum dimension of the pore [56]. It is given by Eq. (7):

$$\Omega = \frac{V_{\text{pore}}}{\frac{4}{3} \cdot \pi \cdot R_{\text{pore}}^3} \quad (7)$$

where  $R_{\text{pore}}$  is the maximum pore radius.

In this study, sphericity ( $\Psi$ ) and compactness ( $\Omega$ ) are used to classify pores. Fig. 5 represents the distribution of all pores in samples 5, 7, 9, 16, 21, 22, 23, 31, and 39 based on sphericity ( $\Psi$ ) and compactness ( $\Omega$ ). The size of points in Fig. 5 represents the diameter of porosities, and as can be seen, porosities with higher compactness and sphericity have a lower diameter. The classification criteria are mentioned in Table 3, which divides spherical pores into six classes (A–F). As shown in Table 3, classes A, B, and C represent spherical pores, whereas classes D, E, and F indicate non-spherical shapes, representing irregularly shaped porosities. Combined with information about pore size, it is also possible to classify pore types, such as GIPs and KHs. The pore size is determined by the maximum pore diameter of a sphere surrounding the pore. Illustrations of different possible spherical pore shapes (classes A–F) are shown in Fig. 6. Fig. 5 also provides the specific shape characteristics of different porosity classes, along with corresponding values for sphericity and compactness. Pores with a compactness lower than 0.2 and a sphericity lower than 0.45 exhibit irregular shapes that are observed across different samples.

The analysis of pore geometry, including features with  $\Omega \geq 0.2$  and  $\Psi \geq 0.45$  for spherical porosities and features with  $\Omega < 0.2$  and  $\Psi < 0.45$  for irregular shape porosities in all samples, as depicted in Fig. 5 and Fig. 6, provides a comprehensive insight into the microstructural characteristics. As shown in Fig. 6, classes A, B, and C, represented by red, blue, and green, exhibit a high level of sphericity

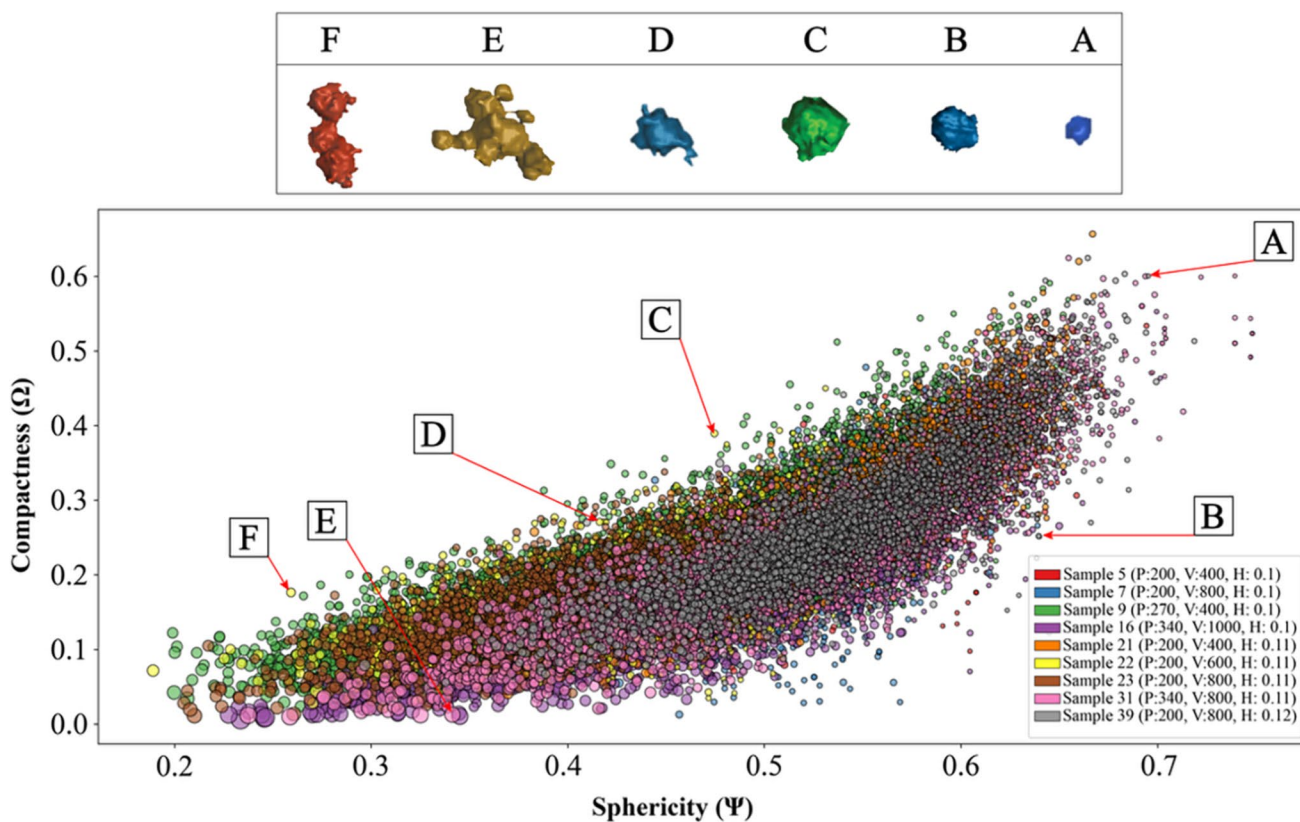


**Fig. 5.** Distribution of spherical (classes A, B, and C) and irregular (classes D, E, and F) pores in certain samples based on sphericity ( $\Psi$ ) and compactness ( $\Omega$ )

**Table 3** Spherical pore classification criteria using x-ray data [56]. Reproduced with permission under a Creative Commons Attribution 4.0 International license, <https://creativecommons.org/licenses/by/4.0/>

Pore class		Diameter	Compactness ( $\Omega$ )	Sphericity ( $\Psi$ )
Spherical	A	$D_{\text{pore}} \leq 100 \mu\text{m}$	$\Omega \geq 0.2$	$\Psi \geq 0.45$
	B	$100 \mu\text{m} < D_{\text{pore}} \leq 200 \mu\text{m}$	$\Omega \geq 0.2$	$\Psi \geq 0.45$
	C	$D_{\text{pore}} > 200 \mu\text{m}$	$\Omega \geq 0.2$	$\Psi \geq 0.45$
Irregular-shaped	D	$D_{\text{pore}} \leq 100 \mu\text{m}$	$\Omega < 0.2$	$\Psi < 0.45$
	E	$100 \mu\text{m} < D_{\text{pore}} \leq 200 \mu\text{m}$	$\Omega < 0.2$	$\Psi < 0.45$
	F	$D_{\text{pore}} > 200 \mu\text{m}$	$\Omega < 0.2$	$\Psi < 0.45$

( $\Psi \geq 0.45$ ) and compactness ( $\Omega \geq 0.2$ ), indicating that these pores are nearly perfect spheres with minimal irregularities. Conversely, classes D, E, and F, shown in purple, orange, and pink, have low sphericity ( $\Psi < 0.45$ ) and compactness ( $\Omega < 0.2$ ). Although these pores are the smallest and least uniform category, their properties align with the expectations for high-density materials. In addition to the classifications presented in Table 3, two specific regions, pores with  $\Psi < 0.45$  and  $\Omega \geq 0.2$  and those with  $\Psi \geq 0.45$  and  $\Omega < 0.2$ , require further analysis. These regions are not explicitly categorized in the table, as their classification requires additional geometric indicators, such as the bounding box factor, in addition to compactness and sphericity. Without incorporating the compactness criterion, pores in the  $\Psi \geq 0.45$  and

$\Omega < 0.2$  region would be mistakenly classified as spherical despite their irregular structural characteristics. Similarly, without considering sphericity, pores in the  $\Psi < 0.45$  and  $\Omega \geq 0.2$  region would also be misclassified as spherical. Therefore, a more comprehensive evaluation integrating multiple shape descriptors is essential for accurately distinguishing pore morphology and reliable porosity classification [56]. The analysis of pore geometry, mainly through metrics such as sphericity and compactness, provides valuable insights into the uniformity and quality of AM components. Higher values of these indicators suggest well-defined, consistent pore structures, contributing to greater material homogeneity. This analysis enables a more precise correlation between porosity and material performance,

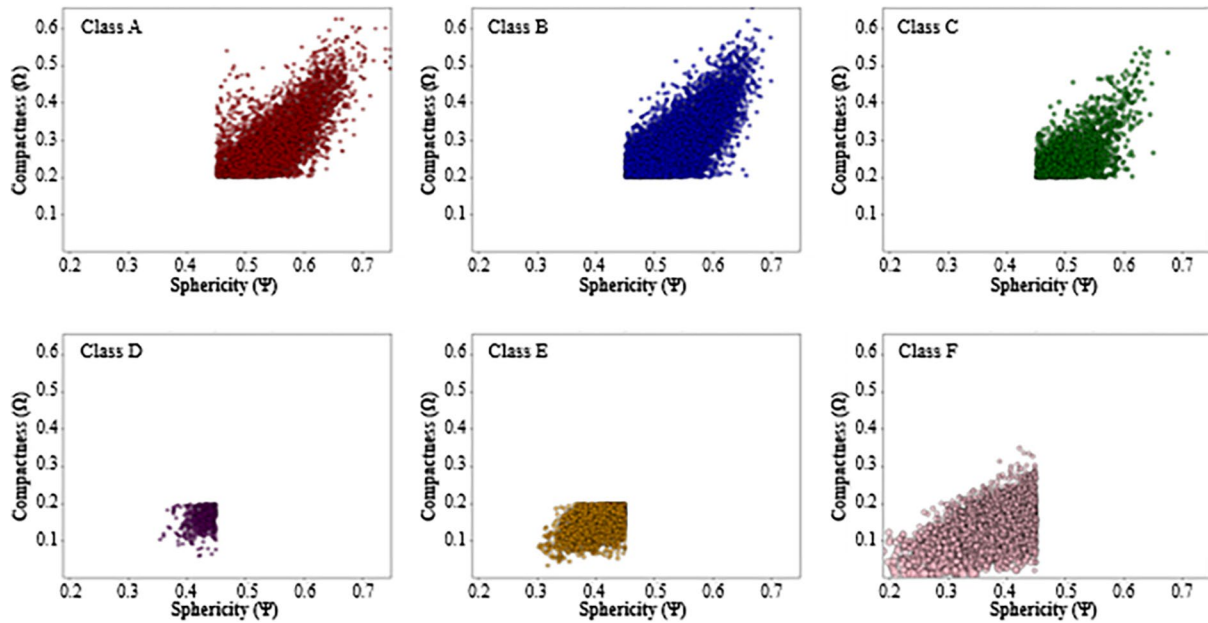


**Fig. 6.** Classification of pores based on sphericity ( $\Psi$ ) and compactness ( $\Omega$ ) parameters. Classes A–C correspond to nearly spherical pores with high  $\Psi$  ( $\geq 0.45$ ) and  $\Omega$  ( $\geq 0.2$ ), and classes D–F exhibit

irregular or elongated morphologies with lower sphericity and compactness. The color of each class matches its corresponding distribution in Fig. 5

aiding process optimization to enhance density, mechanical strength, and structural integrity.

Moreover, Fig. 7 illustrates the pore diameter and sphericity distributions for three samples (13, 31, and 52) processed with different VED values (283, 129, and 49 J/mm<sup>3</sup>, respectively). The results, represented through OM images and 3D pore structures, provide important information on the impact of different VED values on pore shape, relative density, and the overall quality of components produced by (L-PBF). Sample 13 has the lowest relative density at 95.45%, due to the presence of significant GIPs. The distribution of pore diameters is broad, coupled with lower sphericity values, indicating that the pores are irregular and unevenly distributed. The excessive input energy destabilized the melt pool, causing extensive vaporization and GIPs, as evident in the image and 3D representations [57]. Sample 31 shows improvement in relative density, reaching 97.76%. The pore distribution is narrower, and the sphericity is higher, signifying more uniform and controlled porosity. This moderate input energy level creates a stable melt pool, reducing pore formation and enhancing structural consistency. Sample 52 achieves the highest relative density of 99.04%, as its pores are small and perfectly spherical. The low energy input prevented excessive vaporization while providing adequate melting, resulting in an almost defect-free structure. The results highlight the key role of VED in controlling the porosity and achieving high-density components in L-PBF. High values of VED can lead to complications in the melt pool, potentially

resulting in increased porosity content in the final product. Conversely, a well-optimized VED range leads to better outcomes, emphasizing the importance of process parameter optimization in AM processes to achieve the desired mechanical properties, verify dimensional accuracy, and minimize defects [58]. The optimal VED range for this specific alloy seems to be between 40 J/mm<sup>3</sup> and 80 J/mm<sup>3</sup>, as depicted in Fig. 3.

The main effects plot for relative density, derived from XCT, illustrates the significant influence of processing parameters such as power, scanning speed, and hatch distance on the defect content within the samples (Fig. 8). Hatch distance appears to have the most significant influence on the relative density of the processed material, followed closely by the scan speed. In contrast, power has a more moderate effect on relative density. For hatch distance, a clear trend is observed, where an increase from 0.10 mm to 0.11 mm leads to a notable improvement in relative density. As the hatch distance increases to 0.12 mm and 0.13 mm, the relative density improves, due to better energy distribution that enhances the melting process [51]. This analysis aligns with the Archimedes method, where hatch distance also had the most significant impact. However, the XCT results reveal a more linear increase in relative density due to its sensitivity to subsurface porosities. Regarding scan speed, at lower speeds (400 mm/s), the relative density tends to be lower due to the high input energy, which can result in KH effects or instability within the melt pool. However, as the scan speed increases to 600 mm/s and 800 mm/s, the relative density

**Fig. 7.** Pore diameter and sphericity distribution for samples 13 (a), 31(b), and 52 (c) with corresponding OM images and 3D pore representations. Sample 52 shows KH, and sample 13 exhibits GIP, demonstrating the influence of process parameters on pore type and density

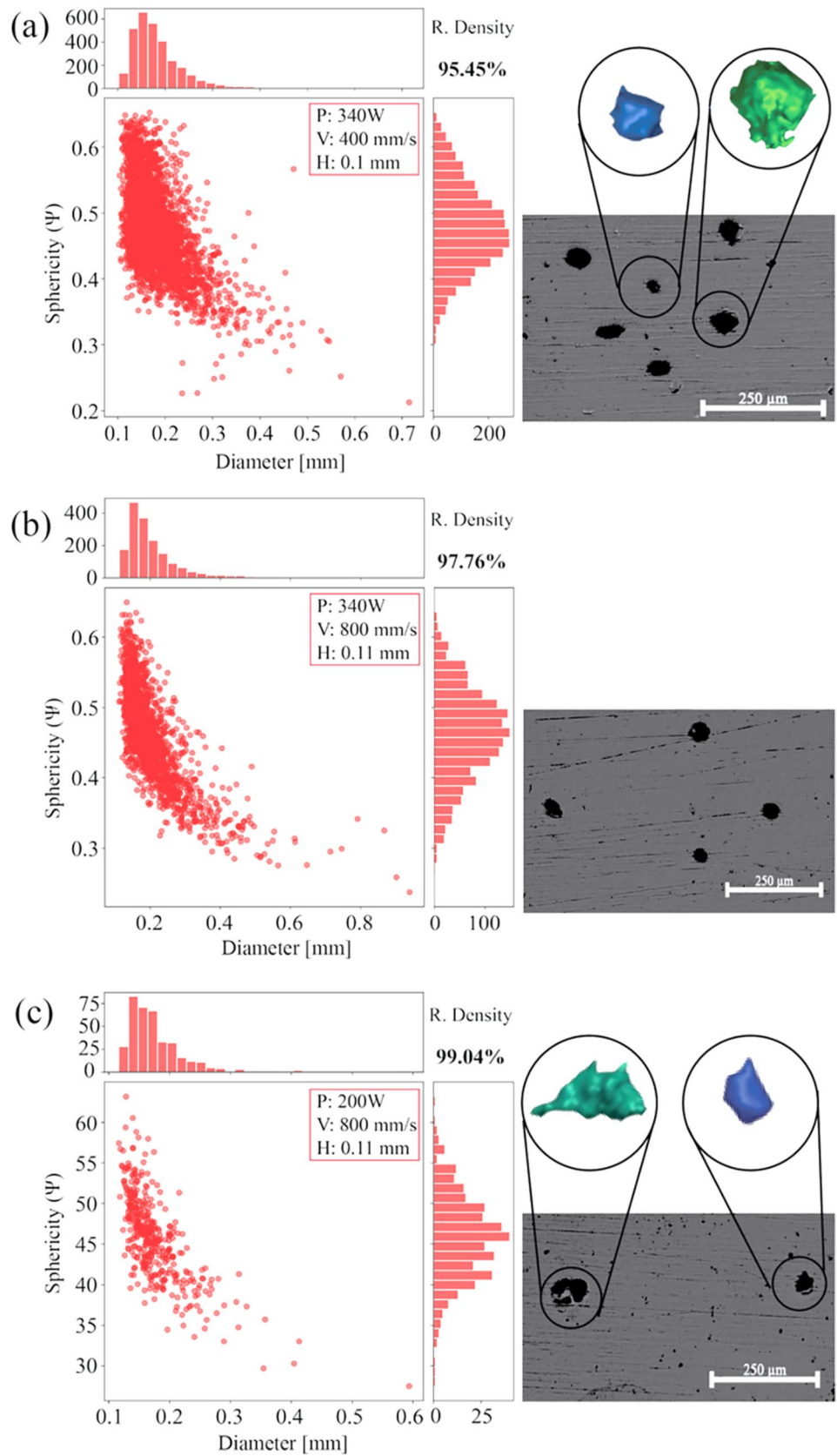
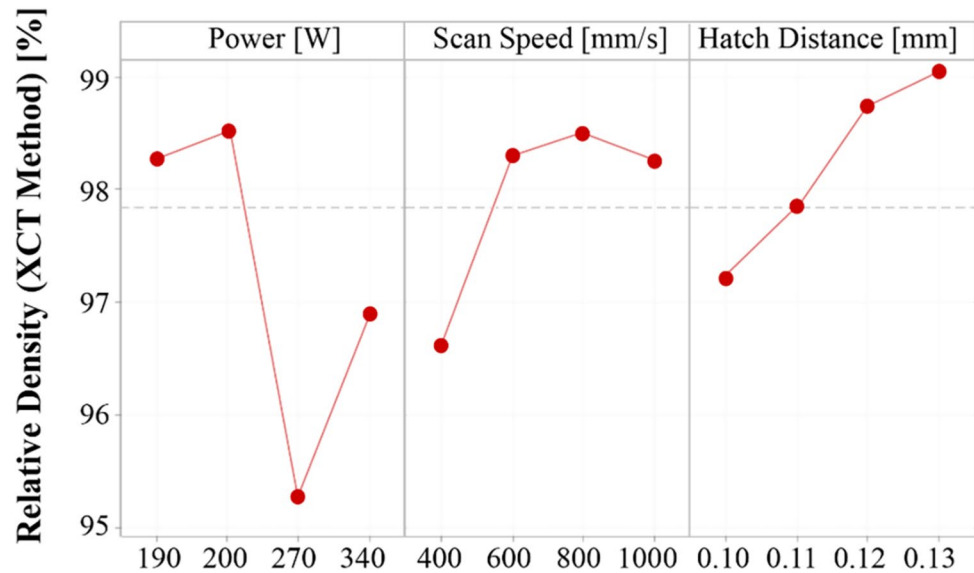


**Fig. 8.** Main effects plot for relative density obtained by XCT as a function of power, scan speed, and hatch distance



reaches its peak, achieving an optimal balance between input energy and defect content. A slight reduction in relative density is observed at 1000 mm/s, where insufficient energy input causes LOF [52]. This trend confirms the results of the Archimedes method, although the XCT analysis highlights a narrower optimal range, showing its higher resolution in detecting porosity. In contrast, power moderately affects relative density, with a nonlinear trend. An increase in power from 190 W to 200 W slightly enhances relative density, indicating an improved melting process. However, a sharp decrease in defect content is observed at 270 W, due to higher energy, which causes GIPs. At a power setting of 340 W, there is a notable enhancement in relative density, which can be attributed to the improved stability of the melt pool at elevated energy levels [54].

It was worth to be mentioned that XCT method has important practical limitations that must be acknowledged when applying it to AM components. Effective spatial resolution, contrast, and defect detectability depend strongly on sample size, geometry, and material density. Larger or thicker parts increase x-ray attenuation and scatter, reduce signal-to-noise ratio, and constrain geometric magnification (thus increasing voxel size), so the sub-100  $\mu\text{m}$  sensitivity achievable on small coupons is often unattainable for full-scale components. In addition, beam-hardening, scatter, ring artifacts, motion blur, and partial-volume effects can create false features or obscure small pores/cracks, while segmentation and reconstruction choices introduce further uncertainty in defect sizing and volume fraction measurements.

Practical consequences include long scan times, large data volumes, and limited throughput for production inspection, as well as restricted accessibility to higher-energy or synchrotron sources that would help penetrate dense parts.

To mitigate these shortcomings, practitioners commonly image representative coupons or use region-of-interest/local tomography, employ higher-energy sources or phase-contrast techniques where available, apply careful artifact correction and validated segmentation workflows, and combine XCT with complementary NDE methods (ultrasonics, eddy current) or destructive validation (metallography) [59–61].

A microscopic analysis was conducted to facilitate a more comprehensive investigation of porosity formation. Fig. 9 illustrates the microstructures of four samples subjected to varying VED values during the L-PBF processing of AISI 316L-Cu. The micrographs reveal a combination of equiaxed and columnar cellular structures of differing sizes, attributable to variations in thermal history and cooling rates, thereby highlighting the distinctive grain morphology characteristic of the L-PBF technique.

In point of view of metallurgical defects, cracks observed near the melt pools were found to propagate during fabrication when employing VED values (Fig. 9a). It has been documented that larger melt pools formed at elevated VED levels exhibit an increased tendency for the formation of solidification micro-shrinkage porosity [23, 62]. For samples processed with lower VED values, porosity was characterized by prominent cavities containing loosely adhered particles (Fig. 9b and c). This finding suggests that these particles are likely partially unmelted powder particles. A plausible explanation for this phenomenon is that a lower laser energy density reduces the melt pool size, resulting in incomplete melting of powder particles and inadequate bonding between successive layers. Conversely, samples fabricated with optimized VED values (Fig. 9d) demonstrated a negligible porosity and no metallurgical defects, such as pores or cracks.

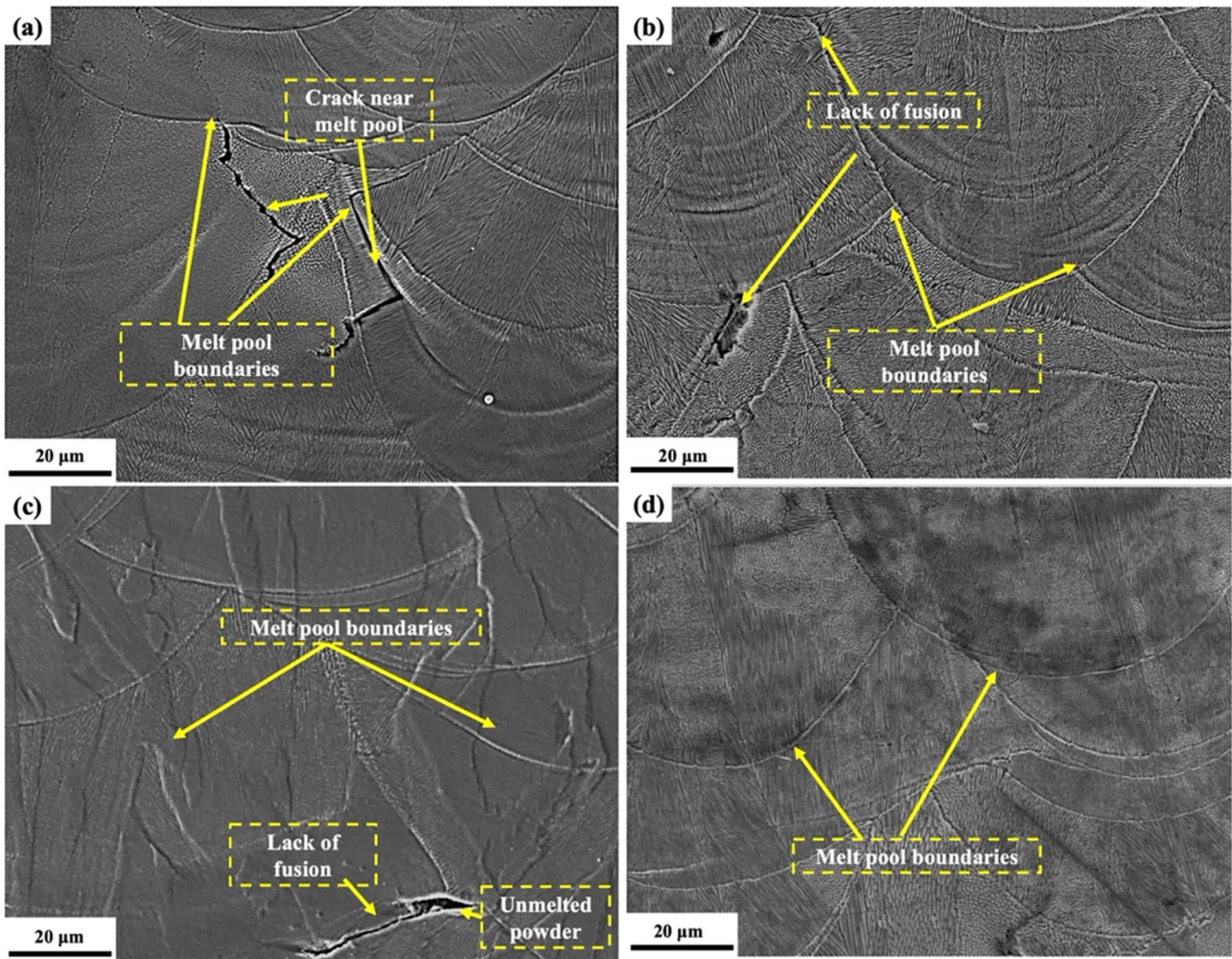


Fig. 9. SEM micrographs of the as-built AISI 316L-Cu for a sample 16, b sample 5, c sample 21, and d sample 52

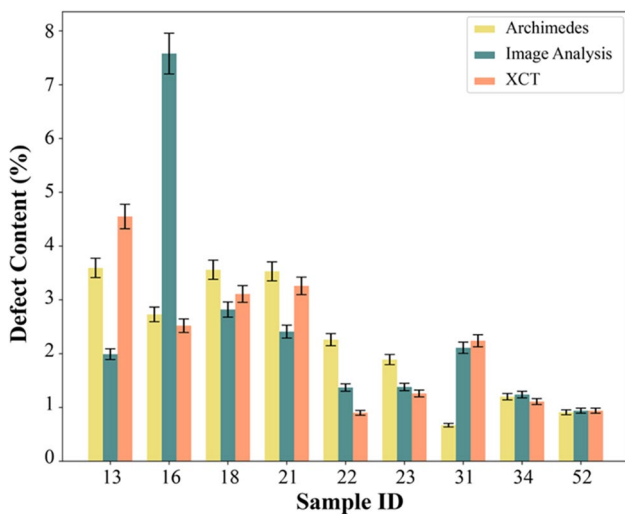
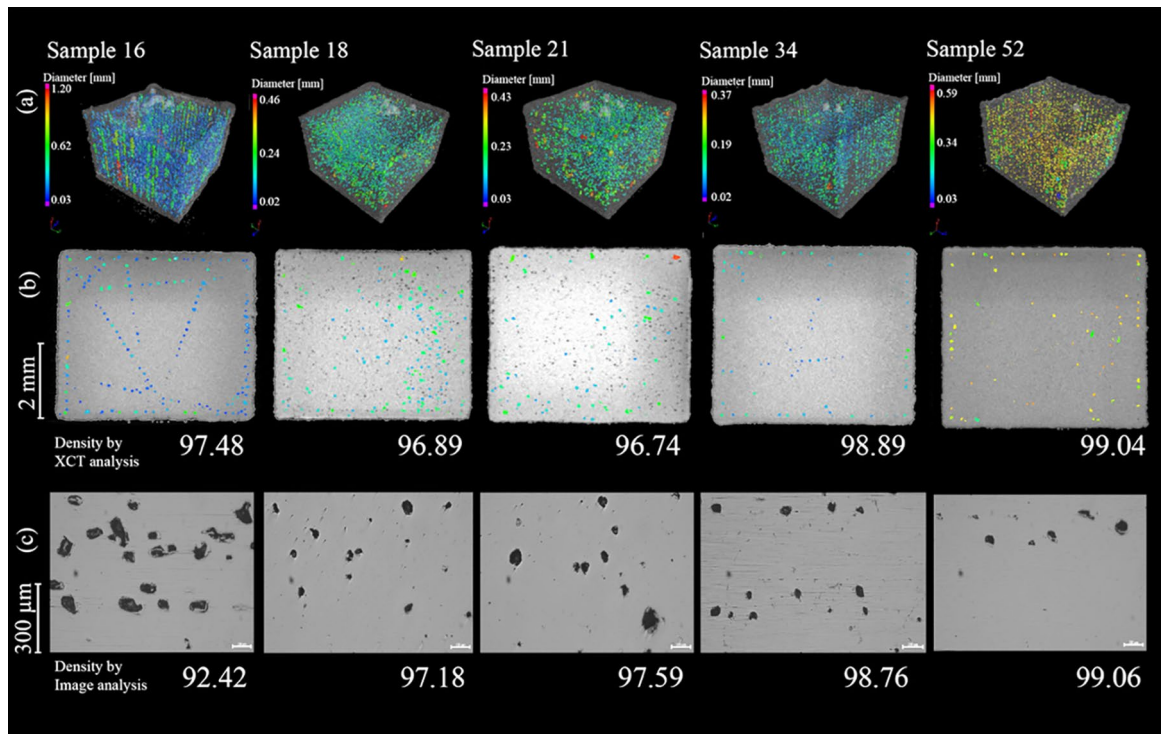


Fig. 10. Porosity analysis of L-PBF samples using Archimedes density, XCT, and image analysis

### Method Comparison

The porosity of the samples was evaluated using Archimedes density method, XCT, and image analysis, each providing unique advantages and limitations in terms of accuracy, resolution, and applicability. Fig. 10 illustrates the differences in defect content across samples as determined by statistical analysis. Sample 16 shows a significant variation in porosity content as measured through image analysis. The higher porosity observed in image analysis may be caused by the specific cross section selected for evaluation, which contains a higher concentration of defects. Since image analysis is limited to a two-dimensional perspective, different cross sections may yield varying porosity values, introducing uncertainty in the measurement. This variability highlights a key limitation of the method. XCT demonstrates fewer pores in the bulk, highlighting its capacity to capture 3D pore structures. In the case of samples with higher densities, such as Sample 52, the results from



**Fig. 11.** Analysis of the relative density of the samples employing various density measurement techniques. **a** presents the 3D tomography, providing a comprehensive visualization of the sample structure, with each sample measuring  $8 \times 8 \times 8$  mm, **b** emphasizes the frontal

perspective of the samples, displaying internal characteristics via tomography imaging, **c** presents images acquired through OM

all three methods indicate close alignment, highlighting reduced fluctuations and enhanced reliability. A comprehensive visual comparison discussing porosity distribution is shown in Fig. 11. 3D tomography corresponds to the location and shape of pores, indicating significant porosity content in Sample 16, while Sample 52 has a dense and uniform structure. The 2D CT images confirm a consistent pore distribution in dense samples, whereas Sample 16 displays significant surface defects.

This analysis highlights the limitations of Archimedes and image analysis in identifying specific and subsurface porosity, while XCT provides a comprehensive 3D representation of pore structure and distribution. All three processes yield consistent outcomes for components with low porosity, demonstrating their reliability with optimized process parameters. Our results align closely with observations reported by other researchers [38, 42, 63, 64], confirming that the trends identified in this study are consistent with those found in the broader literature. In the study done by Zheng et al. [38], a close alignment among the techniques at high relative densities was found. XCT generally reported slightly higher density values, although the authors highlighted that its resolution limit of approximately  $5 \mu\text{m}$  may lead to the omission of smaller

pores, reflecting the same balance between bulk accuracy and three-dimensional sensitivity discussed in this study. In their study, hatch distance had the greatest impact on relative density, followed by laser power and scan speed, which further supports our findings by demonstrating a similar hierarchy of process parameter effects. Similarly, Spierings et al. [63] conducted a direct comparison of the Archimedes method, metallographic analysis, and XCT. Their results showed that the Archimedes technique provides high accuracy and repeatability for samples with high relative density, while 2D image analysis depends strongly on the selected section and the magnification used. They found that although XCT allowed visualization of the three-dimensional pore structure, its detectability threshold may overestimate density by missing the smallest pores, particularly in nearly fully dense specimens. These findings are consistent with the results of our study, confirming that while Archimedes and image analysis methods are reliable for analyzing bulk porosity, XCT is still required to accurately characterize the 3D morphology and distribution of pores within the material.

In AM, XCT scans are known for their considerable costs compared to other measurement techniques like the Archimedes method and image analysis. This observation

suggests that if alternative methodologies can provide sufficiently accurate assessments of the internal geometry of components, the overall costs related to verification processes may be significantly reduced. De Chiffre et al. [65] conducted an extensive analysis regarding the utilization of XCT across various industries, including AM. They identified several key challenges and obstacles such as issues with measurement accuracy, the handling of large and high-density components, the signal-to-noise ratio, the effectiveness of reconstruction algorithms, the need for task-specific measurement configurations, the complexities of multi-material assessments, setup durations, measurement uncertainties, in-line measurement capabilities, and the overall high costs involved. In another study conducted by Turner et al. [66], the application of XCT in AM was compared to other nondestructive evaluation (NDE) methods, such as x-ray imaging, ultrasonic testing, and acoustic resonance testing. The authors identified several barriers to XCT, including limited standardization, large data volumes, high system costs, insufficient understanding of system capabilities, and the need for personnel certification. The study concluded that XCT presents an alternative solution for NDE, mainly due to the absence of standardized specifications for either AM or XCT, which represents a significant technological barrier.

With the progress of computer vision technologies, several studies have focused on analyzing powder bed defects from in situ SLM images and using these datasets to train machine learning models that can automatically detect such defects [67]. As an example, Power et al. [68] investigated unsupervised and semi-supervised machine learning methods for real-time defect detection in Ti-6Al-4 V lattice structures fabricated by L-PBF. They analyzed in situ photodiode data from the melt pool using the STRAY anomaly detection algorithm and one-dimensional autoencoder (1-DAE). The study demonstrated that the 1-DAE achieved superior performance and exhibited strong generalization across different geometries and build platforms, while maintaining millisecond-level inference time. Their results further support the growing trend toward real-time, data-driven anomaly detection in L-PBF using minimally labeled or unlabeled sensor data, aligning closely with the objectives of our current work. Galarza et al. [69] developed a machine learning framework for real-time pore detection in L-PBF using mean light intensity data from the optical tomography system of an EOS M290. They trained several models and found that a simple neural network achieved about 87% accuracy with real-time prediction capability. Their work demonstrates the feasibility of integrating lightweight machine learning models into L-PBF systems for rapid, in situ defect detection. Future research should focus on the connection between pore characteristics and various mechanical properties of parts, emphasizing

strategies for reducing measurement costs, such as machine learning. By prioritizing cost-effective methods, researchers can improve the feasibility and accessibility of accurate assessments, ultimately leading to enhanced performance and reliability in AM.

## Conclusion

- The study concludes that Archimedes and image analysis methods effectively evaluate overall porosity but are insufficient for identifying localized and subsurface porosities. Although these methods provide important insights, they require additional development for more comprehensive porosity characterization.
- The results from all three methods show consistency in evaluating samples with higher densities, indicating their reliability under optimal conditions.
- XCT has shown its effectiveness in analyzing pore distribution, shape, and size in 3D, providing more detailed information than conventional techniques. By using shape indicators like sphericity and compactness, XCT enables accurate classification of spherical pores and provides more accurate assessments of material quality.
- From the porosity geometry analysis, it was observed that a specific optimized energy input range, as was shown by VED in the range of 38–70 J/mm<sup>3</sup>, improved structural integrity, reducing the risk of excessive porosity.
- The correlation between process parameters and relative density is essential for optimizing the quality of components produced by L-PBF.
- Main effects plot analysis confirms that hatch distance has the greatest influence on relative density, followed by scan speed, while power shows a moderate effect.

**Funding** Open access funding provided by Politecnico di Torino within the CRUI-CARE Agreement.

**Open Access** This article is licensed under a Creative Commons Attribution 4.0 International License, which permits use, sharing, adaptation, distribution and reproduction in any medium or format, as long as you give appropriate credit to the original author(s) and the source, provide a link to the Creative Commons licence, and indicate if changes were made. The images or other third party material in this article are included in the article's Creative Commons licence, unless indicated otherwise in a credit line to the material. If material is not included in the article's Creative Commons licence and your intended use is not permitted by statutory regulation or exceeds the permitted use, you will need to obtain permission directly from the copyright holder. To view a copy of this licence, visit <http://creativecommons.org/licenses/by/4.0/>.

## References

- S. Srivastava, R.K. Garg, V.S. Sharma, N.G. Alba-Baena, A. Sachdeva, R. Chand et al., Multi-physics continuum modelling approaches for metal powder additive manufacturing: a review. *Rapid Prototyp. J.* **26**(4), 737–764 (2020)
- Mosallanejad MH, Ghanavati R, Behjat A, Taghian M, Saboori A, Iuliano L. Untapped Opportunities in Additive Manufacturing with Metals: From New and Graded Materials to Post-Processing. *Metals* (Basel). 2024 Apr 3; 14(4):425. Available from: <https://www.mdpi.com/2075-4701/14/4/425>
- M. Attaran, The rise of 3-D printing: the advantages of additive manufacturing over traditional manufacturing. *Bus. Horiz.* **60**(5), 677–688 (2017)
- A. Moradi, S. Tajalli, M. Mosallanejad, A. Saboori, Intelligent laser-based metal additive manufacturing: a review on machine learning for process optimization and property prediction. *Int. J. Adv. Manuf. Technol.* **136**, 527–560 (2024)
- U.M. Dilberoglu, B. Gharehpapagh, U. Yaman, M. Dolen, The role of additive manufacturing in the era of Industry 4.0. *Procedia Manufacturing.* **11**, 545–554 (2017)
- I. Aiza, C. Baldi, F.M. de la Vega, S. Sebastiani, N.E. Veronese, M. Yousefi et al., Effects of build orientation and inclined features on physical, microstructural and mechanical properties of powder bed fusion additively manufactured metallic parts. *Prog. Mater. Sci.* **147**, 101357 (2025)
- T. DebRoy, H.L. Wei, J.S. Zuback, T. Mukherjee, J.W. Elmer, J.O. Milewski et al., Additive manufacturing of metallic components – process, structure and properties. *Prog. Mater. Sci.* **92**, 112–224 (2018)
- D. Jafari, T. Vaneker, I. Gibson, Wire and arc additive manufacturing: opportunities and challenges to control the quality and accuracy of manufactured parts. *Mater. Des.* (2021). <https://doi.org/10.1016/j.matdes.2021.109471>
- Rathee S, Srivastava M, Maheshwari S, Kundra TK, Siddiquee A. Friction Based Additive Manufacturing Technologies: Principles for Building in Solid State, Benefits, Limitations, and Applications. 2018.
- S.M. Thompson, L. Bian, N. Shamsaei, A. Yadollahi, An overview of direct laser deposition for additive manufacturing; Part I: transport phenomena, modeling and diagnostics. *Addit. Manuf.* **8**, 36–62 (2015)
- A. Moradi, S. Tajalli, A. Behjat, A. Saboori, L. Iuliano, Surface engineering of EB-PBF Ti6Al4V via anodization: multifunctional improvements through TiO<sub>2</sub> nanotube arrays. *Coatings.* **15**(9), 993 (2025)
- S. Eshkabilov, I. Ara, F. Azarmi, A comprehensive investigation on application of machine learning for optimization of process parameters of laser powder bed fusion-processed 316L stainless steel. *Int. J. Adv. Manuf. Technol.* **123**(7–8), 2733–2756 (2022)
- M.R. Bandekhoda, M.H. Mosallanejad, M. Atapour, L. Iuliano, A. Saboori, Investigation on the potential of laser and electron beam additively manufactured Ti–6Al–4V components for orthopedic applications. *Met. Mater. Int.* **30**(1), 114–126 (2024)
- L. Zeng, S. Armstrong, Y. Zhu, S.D. Gregory, A. Huang, J.M. Dyson, 3D-printed surfaces of titanium implant: the fibroblasts response. *Biomater Adv.* **166**, 214006 (2025)
- R. Makeen, K. Joshi, M.H. Jhon, P. Promoppatum, Distortion prediction and geometry compensation using modified inherent strain method for additively manufactured Ti-6Al-4V. *J. Manuf. Process.* **131**, 1334–1347 (2024)
- S. Alipour, M. Habibnejad Korayem, A. Emdadi, Laser powder bed fusion processing of plasma atomized AlSi10Mg powder: Surface roughness and mechanical properties modification. *J. Manuf. Process.* **131**, 560–568 (2024)
- J. Zhou, M. Li, X. Yang, W. Shen, G. Wu, X. Ming et al., In-situ laser surface remelting of laser powder bed fused AlSi10Mg alloy at argon and nitrogen protective gases: multiscale analysis. *Opt. Laser Technol.* (2025). <https://doi.org/10.1016/j.optlastec.2024.111631>
- T. Gundgire, S. Santa-aho, T. Rautio, M. Vippola, Severe shot peening: a promising solution for mitigating stress corrosion cracking in solution-annealed LPBF 316 L stainless steel. *Mater. Lett.* (2025). <https://doi.org/10.1016/j.matlet.2024.137626>
- A. Behjat, M. Shamanian, L. Iuliano, A. Saboori, Laser powder bed fusion in situ alloying of AISI 316L–2.5%Cu alloy: microstructure and mechanical properties evolution. *Prog Addit Manuf.* (2024). <https://doi.org/10.1007/s40964-023-00557-x>
- D. Gu, Y.C. Hagedorn, W. Meiners, G. Meng, R. Batista, K. Wissenbach et al., Densification behavior, microstructure evolution, and wear performance of selective laser melting processed commercially pure titanium. *Acta Mater.* **60**, 3849–3860 (2012)
- N.T. Aboulkhair, N.M. Everitt, I. Ashcroft, C. Tuck, Reducing porosity in AlSi10Mg parts processed by selective laser melting. *Addit. Manuf.* **1–4**, 77–86 (2014)
- Gong H, Rafi H, Nadimpalli K, Starr T, Stucker B. Defect morphology in Ti-6Al-4V parts fabricated by selective laser melting and electron beam melting. 24th International SFF symposium - an additive manufacturing conference, SFF 2013. 2013.
- Behjat A, Shamanian M, Sadeghi F, Mosallanejad MH, Saboori A. Process-driven structural and property evolution in laser powder bed fusion of a newly developed AISI 316L stainless steel. *Materials* (Basel). 2025 Jul 16; 18(14):3343. Available from: <https://www.mdpi.com/1996-1944/18/14/3343>
- Z. Gu, S. Sharma, D.A. Riley, M.V. Pantawane, S.S. Joshi, S. Fu et al., A universal predictor-based machine learning model for optimal process maps in laser powder bed fusion process. *J. Intell. Manuf.* **34**(8), 3341–3363 (2023)
- A. Moradi, S. Tajalli, M. Taghian, A. Behjat, A. Saboori, L. Iuliano, Enhancing additive manufacturing quality and productivity using machine learning: a study on laser powder bed fusion of AISI 316L–2.5%Cu. *Prog Addit Manuf.* (2025). <https://doi.org/10.1007/s40964-025-01452-3>
- A. Behjat, M. Shamanian, A. Taherizadeh, E. Lannunziata, S. Bagherifard, E. Gadalińska et al., Microstructure-electrochemical behavior relationship in post processed AISI316L stainless steel parts fabricated by laser powder bed fusion. *J. Mater. Res. Technol.* **23**, 3294–3311 (2023)
- Q. Wang, L. Ren, X. Li, S. Zhang, T.B. Sercombe, K. Yang, Antimicrobial Cu-bearing stainless steel scaffolds. *Mater. Sci. Eng. C Biomimet. Mater. Sens. Syst.* **68**, 519–522 (2016). <https://doi.org/10.1016/j.msec.2016.06.038>
- A. Behjat, S. Sanaei, M.H. Mosallanejad, M. Atapour, A. Saboori, Electrochemical behavior of electron beam powder bed fused Ti536 alloy under simulated inflammatory conditions. *Acta Metall Sin (English Lett)*. **38**(6), 969–980 (2025). <https://doi.org/10.1007/s40195-025-01846-w>
- Behjat A, Norouzi E, Kharaziha M, Suh JY, Bagherifard S, Khorramian M, et al. Laser powder bed fusion of copper-bearing AISI 316 L: Microstructure, biofunctional and corrosion performance. *Mater Charact [Internet]*. 2025 Nov;229:115614. Available from: <https://linkinghub.elsevier.com/retrieve/pii/S1044580325009039>
- S. Das, Physical Aspects of Process Control in Selective Laser Sintering of Metals. *Adv. Eng. Mater.* **5**(10), 701–711 (2003)
- Q. Liu, J. Elambasseril, S. Sun, M. Leary, M. Brandt, P. Sharp, The Effect of Manufacturing Defects on The Fatigue Behaviour of Ti-6Al-4V Specimens Fabricated Using Selective Laser Melting. *Adv. Mater. Res.* **891–892**, 1519–1524 (2014)
- T. Vilaro, C. Colin, J.D. Bartout, As-Fabricated and Heat-Treated Microstructures of the Ti-6Al-4V Alloy Processed by Selective

- Laser Melting. *Metall. Mater. Trans. A Phys. Metall. Mater. Sci.* **42**(10), 3190–3199 (2011)
33. H. Gong, K. Rafi, H. Gu, T. Starr, B. Stucker, Analysis of defect generation in Ti–6Al–4V parts made using powder bed fusion additive manufacturing processes. *Addit. Manuf.* **1–4**, 87–98 (2014)
  34. B. Song, S. Dong, Q. Liu, H. Liao, C. Coddet, Vacuum heat treatment of iron parts produced by selective laser melting: Microstructure, residual stress and tensile behavior. *Mater. Des.* **54**, 727–733 (2014)
  35. D. Gu, Y. Shen, Balling phenomena in direct laser sintering of stainless steel powder: metallurgical mechanisms and control methods. *Mater. Des.* **30**(8), 2903–2910 (2009)
  36. A.K. Agrawal, B. Rankouhi, D.J. Thoma, Predictive process mapping for laser powder bed fusion: a review of existing analytical solutions. *Curr. Opin. Solid State Mater. Sci.* **26**(6), 101024 (2022)
  37. C. Qiu, C. Panwisawas, M. Ward, H.C. Basoalto, J.W. Brooks, M.M. Attallah, On the role of melt flow into the surface structure and porosity development during selective laser melting. *Acta Mater.* **96**, 72–79 (2015)
  38. Z. Zheng, L. Peng, D. Wang, Defect analysis of 316 L stainless steel prepared by LPBF additive manufacturing processes. *Coatings.* (2021). <https://doi.org/10.3390/coatings11121562>
  39. J.P. Roth, I. Šulák, T. Kruml, W. Polkowski, T. Dudziak, P. Böhlke et al., Establishing a process route for additive manufacturing of NiCu-based Alloy 400: an alignment of gas atomization, laser powder bed fusion, and design of experiments. *Int. J. Adv. Manuf. Technol.* **134**(7), 3433–3452 (2024)
  40. Z. Men, L. Wang, X. Gao, W. Chen, C. Ji, Z. Li et al., Accurate detection and analysis of pore defects in laser powder bed fusion WE43 magnesium alloys. *Micromachines.* (2024). <https://doi.org/10.3390/mi15070909>
  41. T. Yamamoto, M. Hara, Y. Hatano, Effects of fabrication conditions on the microstructure, pore characteristics and gas retention of pure tungsten prepared by laser powder bed fusion. *Int. J. Refract. Met. Hard Mater.* **95**, 105410 (2021)
  42. N. Nudelis, P. Mayr, Defect-based analysis of the laser powder bed fusion process using X-ray data. *Int. J. Adv. Manuf. Technol.* **123**(9), 3223–3232 (2022)
  43. A. Poudel, M. Yasin, J. Ye, J. Liu, A. Vinel, S. Shao et al., Feature-based volumetric defect classification in metal additive manufacturing. *Nat. Commun.* **13**, 6369 (2022)
  44. X. Wang, L. Zhao, J.Y.H. Fuh, H.P. Lee, Effects of statistical pore characteristics on mechanical performance of selective laser melted parts: X-ray computed tomography and micromechanical modeling. *Mater. Sci. Eng. A.* **834**, 142515 (2022)
  45. B.R. Jolley, M.D. Uchic, D. Sparkman, M. Chapman, E.J. Schwalbach, Application of serial sectioning to evaluate the performance of X-ray computed tomography for quantitative porosity measurements in additively manufactured metals. *JOM.* **73**(11), 3230–3239 (2021)
  46. B. Jolley, C. Knott, D. Sparkman, M. Uchic, Comparative analysis of internal porosity in AM Ti64 using X-ray computed tomography and mechanical polishing serial sectioning. *IEEE Open J. Instrum. Meas.* (2024). <https://doi.org/10.1109/OJIM.2024.3477569>
  47. I. Ara, F. Azarmi, X.W. Tangpong, Microstructure analysis of high-density 316L stainless steel manufactured by selective laser melting process. *Metallogr. Microstruct. Anal.* **10**(6), 754–767 (2021)
  48. Standard Guide for Additive Manufacturing of Metal — Finished Part Properties — Methods for Relative Density Measurement. 10.04:6.
  49. M. Bakhtiarian, H. Omidvar, A. Mashhuriazar, Z. Sajuri, C.H. Gur, The effects of SLM process parameters on the relative density and hardness of austenitic stainless steel 316L. *J. Mater. Res. Technol.* **29**, 1616–1629 (2024)
  50. H.Y. Chia, J. Wu, X. Wang, W. Yan, Process parameter optimization of metal additive manufacturing: a review and outlook. *J Mater Informatics.* **2**, 16 (2022)
  51. Brown C, Jacob G, Possolo A, Beauchamp C, Peltz M, Stoudt M, et al. The Effects of Laser Powder Bed Fusion Process Parameters on Material Hardness and Density for Nickel Alloy 625. *Advanced Manufacturing Series (NIST AMS)*, National Institute of Standards and Technology, Gaithersburg, MD; 2018.
  52. Z. Chen, Y. Lu, F. Luo, S. Zhang, P. Wei, S. Yao et al., Effect of laser scanning speed on the microstructure and mechanical properties of laser-powder-bed-fused K418 nickel-based alloy. *Materials.* (2022). <https://doi.org/10.3390/ma15093045>
  53. Z. Wei, Effects of laser scanning speed on the microstructure and mechanical properties of 2205 duplex stainless steel fabricated by selective laser melting. *J. Manuf. Process.* **94**, 1–9 (2023)
  54. A. Paraschiv, G. Matache, M.R. Condruz, T.F. Frigioescu, L. Pambaguan, Laser powder bed fusion process parameters' optimization for fabrication of dense IN 625. *Materials.* (2022). <https://doi.org/10.3390/ma15165777>
  55. B. Baumgärtner, J. Hussein, T. Hausotte, Investigation of the shape and detectability of pores with X-ray computed tomography. *J. Manuf. Mater. Process.* (2023). <https://doi.org/10.3390/jmmp7030103>
  56. N. Nudelis, P. Mayr, A novel classification method for pores in laser powder bed fusion. *Metals (Basel).* **11**, 1912 (2021)
  57. D.Y. Pimenov, L.F. Berti, G. Pintaude, G.X. Peres, Y. Chaurasia, N. Khanna et al., Influence of selective laser melting process parameters on the surface integrity of difficult-to-cut alloys: comprehensive review and future prospects. *Int. J. Adv. Manuf. Technol.* **127**(3), 1071–1102 (2023)
  58. P. Hanzl, M. Zetek, T. Bakša, T. Kroupa, The influence of processing parameters on the mechanical properties of SLM parts. *Procedia Eng.* (2015). <https://doi.org/10.1016/j.proeng.2015.01.510>
  59. Sun X, Huang L, Xiao BG, Zhang Q, Li JQ, Ding YH, et al. X-ray computed tomography in metal additive manufacturing: A review on prevention, diagnostic, and prediction of failure. *Thin-Walled Struct* [Internet]. 2025 Feb;207:112736. Available from: <https://linkinghub.elsevier.com/retrieve/pii/S0263823124011765>
  60. Kim FH, Pintar AL, Moylan SP, Garboczi EJ. The Influence of X-Ray Computed Tomography Acquisition Parameters on Image Quality and Probability of Detection of Additive Manufacturing Defects. *J Manuf Sci Eng* [Internet]. 2019 Nov 1;141(11). Available from: <https://asmedigitalcollection.asme.org/manufacturing-science/article/doi/https://doi.org/10.1115/1.4044515/958429/The-Influence-of-XRay-Computed-Tomography>
  61. Dewulf W, Bosse H, Carmignato S, Leach R. Advances in the metrological traceability and performance of X-ray computed tomography. *CIRP Ann* [Internet]. 2022;71(2):693–716. Available from: <https://linkinghub.elsevier.com/retrieve/pii/S0007850622001275>
  62. Chandra S, Radhakrishnan J, Huang S, Wei S, Ramamurty U. Solidification in metal additive manufacturing: challenges, solutions, and opportunities. *Prog Mater Sci* [Internet]. 2025 Feb; 148:101361. Available from: <https://linkinghub.elsevier.com/retrieve/pii/S0079642524001300>
  63. A. Spierings, M. Schneider, R. Eggenberger, Comparison of density measurement techniques for additive manufactured metallic parts. *Rapid Prototyp. J.* **17**, 380–386 (2011)
  64. S. Baig, A. Jam, S. Beretta, S. Shao, N. Shamsaei, Non-destructive detection of critical defects in additive manufacturing. *Sci. Rep.* **15**(1), 6740 (2025)
  65. L. De Chiffre, S. Carmignato, J.P. Kruth, R. Schmitt, A. Weckenmann, Industrial applications of computed tomography. *CIRP Ann.* **63**(2), 655–677 (2014)

66. Turner N. A10998-Technology review of x-ray CT for inspection and dimensional metrology: deliverable 1: review of x-ray computed tomography for non-destructive testing applications. MTC (Coventry, UK: Manufacturing Technology Centre); 2015.
67. L. Scime, J. Beuth, Anomaly detection and classification in a laser powder bed additive manufacturing process using a trained computer vision algorithm. *Addit. Manuf.* **19**, 114–126 (2017)
68. J.J. Power, D.P. Dowling, S. Keaveney, C. Hoare, Analysis of unsupervised and semi-supervised machine learning techniques for print defect detection during laser powder bed fusion. *Int. J. Adv. Manuf. Technol.* (2025). <https://doi.org/10.1007/s00170-025-15777-4>
69. J. Galarza, J. Barron, L. Jimenez, T. Oraby, J. Li, F. Ahmed, A machine learning approach to detect pores in laser powder bed fusion additive manufacturing. *Manuf. Lett.* **44**, 985–993 (2025)

**Publisher's Note** Springer Nature remains neutral with regard to jurisdictional claims in published maps and institutional affiliations.